Ukrainian Journal of Physical Optics
ISSUE 2
2027

PHOTONIC HYPERCRYSTALS: MULTISCALE DISPERSION, LOCALIZATION, AND OPTICAL CONTROL. REVIEW

ILLIA FEDORIN*

National Technical University of Ukraine "Igor Sikorsky Kyiv Polytechnic Institute",
37 Beresteiskyi Avenue, Kyiv 03056, Ukraine
*Corresponding author: fedorin.illia@edu.kpi.ua

Received: 11.10.2026

Abstract. This review examines how periodic modulation converts the confined waves of hyperbolic media into collective bands, localized states, and accessible optical responses. Artificial multilayers and patterned natural polariton media are compared through the roles of constituent dispersion, lattice coupling, and termination. The analysis connects these mechanisms to measured band shifts, emitter lifetimes, absorption, and near-field mode maps, with attention to the controls needed to identify the contribution of periodicity. Experiments establish several propagation and localization functions, while theoretical studies extend the design space to nonlinear conversion, gain, nodal bands, and thermal transport. Comparing these levels of evidence reveals a recurring design trade-off: field concentration strengthens local interaction, while dissipation and coupling determine the energy available to a useful output. This framework relates multiscale dispersion design to experimental observables and identifies priorities for finite structures, tunability, and fabrication tolerance.

Keywords: photonic hypercrystals, hyperbolic metamaterials, polaritonic crystals, Bloch modes; optical localization, light–matter interaction

UDC: 535.3
DOI: 10.3116/16091833/Ukr.J.Phys.Opt.2027.02001
This work is licensed under the Creative Commons Attribution International License (CC BY 4.0).

1. Physical concept and scope of photonic hypercrystals

The appeal of a photonic hypercrystal begins with a question of scale: how can a structure much smaller than the free-space wavelength still produce a Bragg band gap? In an ordinary photonic crystal, the lattice acts on waves whose wavelength is comparable to its period [1]. A hyperbolic metamaterial (HMM) supplies a different starting point, supporting electromagnetic modes with large wave vectors and correspondingly short internal wavelengths [2]. Narimanov's photonic hypercrystal (PHC) construction combines these properties through additional periodic modulation of a hyperbolic constituent [3]. The extraordinary-wave dispersion of a uniaxial medium makes the underlying scale difference explicit:

$$\frac{k_\tau^2}{\varepsilon_n}+\frac{k_n^2}{\varepsilon_\tau}=\frac{\omega^2}{c^2}, \qquad \varepsilon_n\varepsilon_\tau<0\,. \tag{1}$$

Here k_n and k_τ are the normal and tangential components of the wave vector, respectively. The optical axis n is normal to the layers of a uniaxial laminate, and τ denotes an in-plane direction. The dimensionless quantities ε_n and ε_τ are the corresponding principal relative permittivities; ω is angular frequency, c is the speed of light in vacuum, and $k_0=\omega/c$ is the free-space wavenumber. Eq. (1) describes a local, nonmagnetic medium in the lossless limit. Opposite signs of the principal permittivities produce an open isofrequency surface and permit components much larger than k_0, referred to here as high-k states.

For such a mode, the internal phase varies on a length scale far shorter than the free-space wavelength $\lambda_0 = 2\pi / k_0$. A larger modulation can therefore scatter it coherently even while the lattice remains subwavelength to an incident beam. This opens a route to organizing strongly confined fields into propagating bands and forbidden intervals. At sufficiently large momentum, the field resolves individual layers and the local continuum approximation loses accuracy. Studies of nonlocality, dipole coupling, and finite HMMs show how constituent discreteness and spatial dispersion bound the accessible spectrum; absorption then weights each mode's contribution to propagation and energy exchange [4–12].

This physical picture suggests a hierarchy of three lengths, $a \ll D \ll \lambda_0$: the fine constituent period a, the PHC superperiod D, and the free-space wavelength. Averaging over a gives the effective hyperbolic response, while retaining D allows the internal waves to exchange reciprocal-lattice momentum. In a one-dimensional lattice, this exchange occurs in multiples of $G = 2\pi / D$; transverse and higher-dimensional patterns extend it to reciprocal-lattice vectors. Recent work on transverse hypercrystals and patterned polariton media shows how the same idea can be implemented through an in-plane lattice [13-15].

PHC development has followed two complementary material routes. Self-assembled composites and patterned metal/dielectric multilayers provided early demonstrations of reconfiguration, emission control, and angular band engineering [16–19]; semiconductor HMM experiments established the constituent negative-refraction response that related designs rely on [20]. In the second route, natural van der Waals materials intrinsically supply hyperbolic phonon polaritons. Patterning hexagonal boron nitride (hBN), α-molybdenum trioxide (α-MoO_3), or their surroundings introduces a lattice that couples these confined waves [13–15, 21–29].

These platforms are connected by the coherent reorganization of a high-k spectrum by a second spatial scale. In classical PHCs, both scales arise from artificial structuring; in natural polariton crystals, the material supplies the confined wave, and the fabricated pattern supplies the lattice. Their different origins matter when choosing a fabrication route or spectral range, yet they lead to a shared question: how does the modulation change propagation, localization, and optical access? Table 1 organizes the platforms around this question and places homogeneous HMMs and patterned anisotropic comparators alongside them as sources of constituent and interface physics.

Table 1. Materials and modulation routes discussed in this review.

Family	High-k medium	Modulation	Characteristic response
Classical PHC	Artificial HMM	Larger layered or in-plane period	Bloch bands, gaps, and phase compensation
Transverse PHC	Hyperbolic polariton waveguide	In-plane lattice	Folded polariton bands and multimode coupling
Hyperbolic polaritonic crystal	Natural hyperbolic material	Holes or patterned substrate	Bloch propagation, resonances, and mode selection
Patterned anisotropic comparator	Anisotropic or hyperbolic medium	Geometry selected for a particular resonance	Constituent, interface, or scattering response used for comparison

Existing reviews establish the material and modal foundations for this comparison. Poddubny and colleagues survey the electrodynamics and applications of hyperbolic metamaterials [2], while Caldwell and colleagues examine hBN photonics [24]. Hu and colleagues organize hyperbolic polariton transport across dimensionalities and include patterned polaritonic crystals among the emerging functions [23]. The present review follows the progression from constituent response through periodic coupling to finite boundaries across both artificial and natural platforms. Comparing these stages makes it possible to identify which measured changes arise from the hyperbolic medium, which require its modulation, and how excitation, dissipation, and extraction determine the resulting optical function.

The two geometries in Fig. 1 make the origin of the confined wave and its periodic modulation explicit. In the artificial laminate, the fine layers create the constituent response; in the patterned polariton medium, that response is intrinsic. Both geometries require the larger lattice to be retained when calculating collective propagation. Table 2 relates each structural scale to its electrodynamic description, including the boundary problem that selects localized modes.

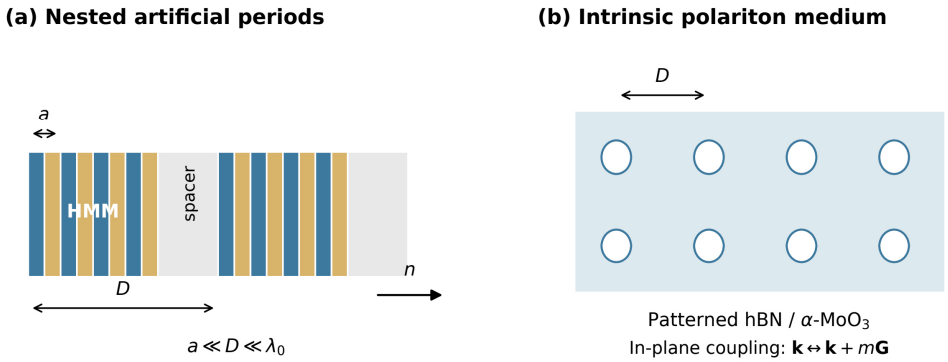


Fig. 1. Original schematic of two routes to a high-k periodic medium. (a) An artificial laminate of period ***a*** forms the hyperbolic constituent; a spacer defines the superperiod ***D***. (b) An intrinsic polariton medium receives an in-plane pattern of period ***D***. The modulation couples internal wave vectors through reciprocal-lattice momentum. Colors and dimensions are schematic; ***n*** is normal to the artificial layers. The cited studies describe these physical constructions [3, 13, 15].

The aim is to relate this hierarchy of scales to evidence that can guide optical design. The discussion first establishes when constituent averaging and explicit Bloch coupling are appropriate, then compares the resulting bands, localized states, and control mechanisms.

Table 2. Structural scales and their electrodynamic descriptions.

Scale	Physical role	Description	Examples
Constituent period a	Anisotropy and high-k propagation	Effective tensor at small internal phase; resolved layers or nonlocal response at large momentum	[4-12, 30-32]
Superperiod D	Coherent mode coupling, gaps, and angular phase control	Bloch or full-wave model retaining the lattice; classically $a \ll D \ll \lambda_0$	[3, 30, 33, 34]
Termination/ defect	Localization, hybridization, and radiation	Finite-stack scattering, surface impedance, and boundary matching	[35-45]

Emission, absorption, and near-field measurements provide the experimental basis for assessing these mechanisms; nonlinear, active, thermal, and inverse-design studies extend the comparison to proposed functions. Throughout, the relevant question is how a calculated mode becomes a measurable response in a finite structure. This connects the review's scope to the choice of model, platform, and experimental control.

2. Effective media and resolved multiscale electrodynamics

The first modeling step is to identify the waves supplied by the constituent. In a classical PHC, this constituent often consists of finely stratified metal/dielectric or semiconductor/dielectric layers. Their contrasting responses allow the electric field parallel to the layers and the field normal to them to experience different averages. For local scalar permittivities ε_1 and ε_2 in a nonmagnetic laminate, the quasistatic arithmetic and harmonic averages give

$$\varepsilon_\tau = f\varepsilon_1 + (1-f)\varepsilon_2, \qquad \varepsilon_n = \left[\frac{f}{\varepsilon_1} + \frac{1-f}{\varepsilon_2}\right]^{-1}. \tag{2}$$

Here, f is the volume fraction of constituent 1 and 1-f that of constituent 2; ε_1 and ε_2 are their scalar relative permittivities. The arithmetic average ε_τ applies parallel to the layers and the harmonic average ε_n normal to them. This quasistatic effective-medium theory (EMT) shows how composition can create opposite signs in the effective tensor. Ali used this fine-laminate description for PHC propagation [30], while ferrite–semiconductor calculations extend the constitutive response to magnetic and gyrotropic media [31]. These averages supply the constituent waves; retaining the larger period then determines how those waves couple.

At the supercell scale, the central question becomes how the constituent waves couple from one period to the next. For a one-dimensional lattice of period $\boldsymbol{D}$, the one-period transfer operator $M(D)$ advances the tangential-field state through one cell. Its Bloch eigenvalues λ_n determine the normal Bloch wavenumbers K_n:

$$\det\left[M(D) - \exp(iKD)I\right] = 0, \qquad \lambda_n = \exp\left(iK_nD\right). \tag{3}$$

In Eq. (3), I is the identity matrix of the same dimension as $M(D)$, K denotes a trial Bloch wavenumber, and the subscript n enumerates eigenmodes. This mode index is distinct from the spatial-axis label in Eq. (1). The imaginary unit is i, and the time dependence is $\exp(-i\omega t)$. Complex Bloch wavenumbers describe absorbing or active media. For a polarization-decoupled system represented by a unimodular 2×2 transfer matrix, the characteristic equation reduces to

$$\cos(KD) = \frac{1}{2}\operatorname{Tr} M(D) \tag{4}$$

Here K is the Bloch wavenumber for the selected polarization, and Tr is the matrix trace. The identity follows from $\det M(D) = 1$, including complex matrix entries. With a real half-trace in a lossless system, $\left|\operatorname{Tr} M(D)/2\right| \le 1$ identifies a pass band, and larger magnitudes identify a stop band. Absorption or gain gives complex K, whose real and imaginary parts describe phase accumulation and attenuation or amplification. Coupled polarizations require the full operator spectrum. In Fig. 2, $M_D \equiv M(D)$ denotes the supercell matrix and $M_a \equiv M(a)$ the fine-cell matrix.

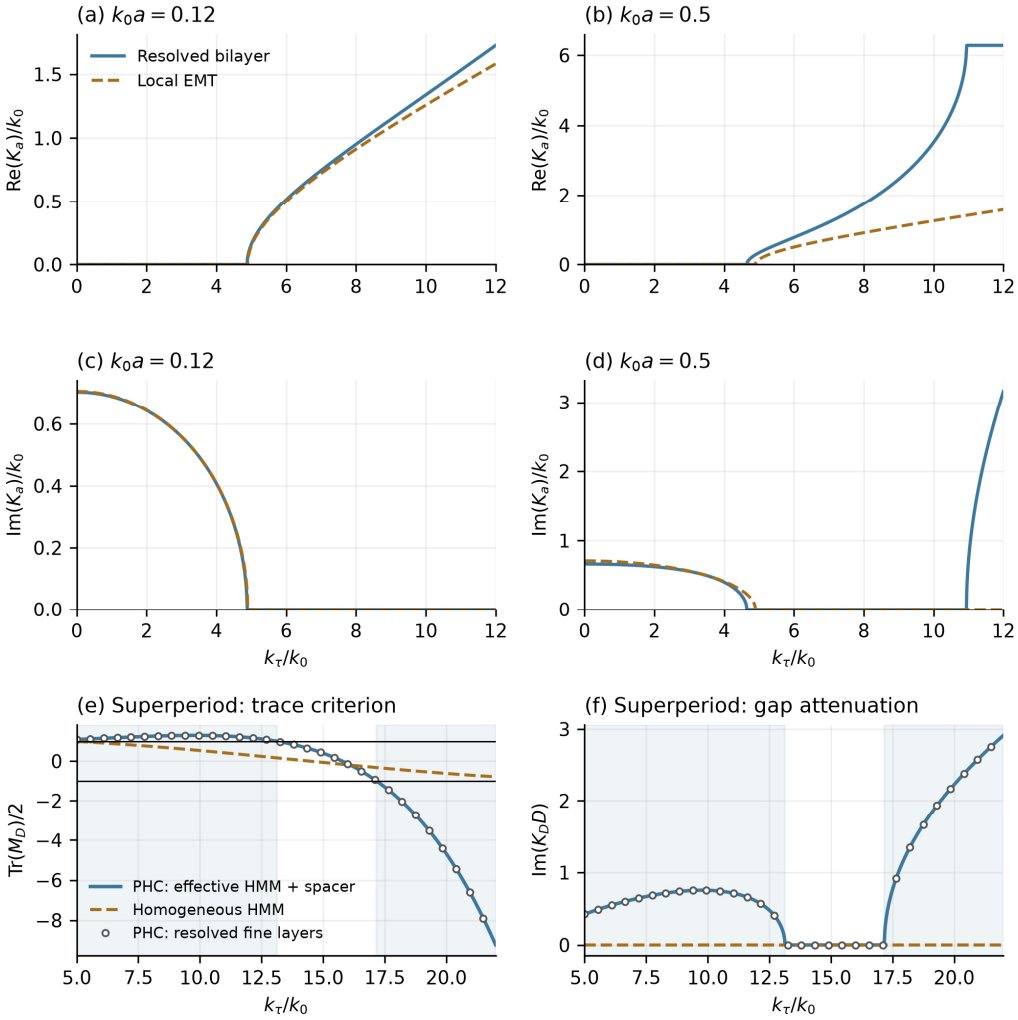


Fig. 2. Original lossless TM calculations comparing constituent homogenization and superperiod coupling at fixed frequency. TM denotes transverse magnetic polarization. (a–d) A bilayer with metal relative permittivity $\varepsilon_m = -4$, dielectric relative permittivity $\varepsilon_d = 3$, and metal filling fraction 0.5 is compared with its local EMT tensor, $\varepsilon_\tau = -0.5$ and $\varepsilon_n = 24$, for $\boldsymbol{k_0 a} =$ 0.12 and 0.5. (e–f) An effective HMM block of thickness $0.8\boldsymbol{D}$ is followed by a dielectric spacer with relative permittivity 3 and thickness $0.2\boldsymbol{D}$, with $\boldsymbol{k_0 D} =$ 0.8. Shading marks momentum gaps where $|\mathbf{Tr}\boldsymbol{M_D}/2|>1$, with $\boldsymbol{M_D} = \boldsymbol{M}(\boldsymbol{D})$ as in Eq. (4). The upper gap starts at $\boldsymbol{K_D D} = \pi$. Open circles sample the resolved result with 256 fine bilayers per HMM block ($\boldsymbol{k_0 a} =$ 0.0025); their overlap with the solid curve shows convergence. $\boldsymbol{K_a}$ and $\boldsymbol{K_D}$ are normal Bloch wavenumbers for periods $\boldsymbol{a}$ and $\boldsymbol{D}$. First-zone phase representatives satisfy $0 \le \mathbf{Re}(\boldsymbol{KL}) \le \pi$ and $\mathbf{Im}(\boldsymbol{KL}) \ge 0$, with $\boldsymbol{L=a}$ or $\boldsymbol{D}$; energy-flow direction follows the modal Poynting flux. Parameters are illustrative. Calculation code, numerical checks, and literature tables: https://doi.org/10.5281/zenodo.23302061.

Fig. 2 compares constituent averaging with superperiod coupling through an illustrative calculation. In panels (a–d), a resolved lossless bilayer approaches the local EMT limit as the phase accumulated within each constituent cell becomes small; the constituent-layer phase, material contrast, and proximity to resonance jointly determine accuracy. Panels (e–f) add a dielectric spacer to the effective hyperbolic block. The homogeneous HMM supports propagation across the plotted momentum interval, while the modulated structure develops gaps. Resolving

progressively finer layers within each block recovers the effective-block result; open markers make this convergence visible. This distinction follows the homogenization analyses [4, 5]: averaging provides a constitutive approximation, and retaining the superperiod provides the additional Bloch coupling. Ferrite–semiconductor and graphene–hBN studies illustrate these complementary modeling choices [31, 32].

As the wavelength decreases further, the field samples the constituent cell more directly. Studies of nonlocal propagation, emitter coupling, and finite HMMs show how spatial dispersion changes the available high-k modes [4-12]. Resolved-layer calculations or a nonlocal constitutive model capture these changes. Including absorption gives the distance over which a wave can propagate and the resonance linewidth, making it possible to assess how much of the designed spectrum remains accessible in a finite sample.

An experiment introduces another step: an incident field must enter a finite structure, excite its modes, and leave through an observable channel. Thickness and termination influence this process through leakage and boundary phase, which can also select surface states, Tamm resonances, and defect modes. Finite-stack transfer matrices, scattering matrices, and full-wave calculations connect the bulk spectrum to reflection, transmission, and the spatial field distribution. This connection becomes especially important when a band feature is used to concentrate energy in a device.

Distributed-feedback lasing illustrates why constituent resolution can affect device predictions. In the PHC model considered by Janaszek and Szczepański, nonlocal corrections shift Bragg wavelengths, polarization behavior, and calculated lasing thresholds [46]. Changes in the complex dispersion alter where feedback occurs and how the field overlaps gain, loss, and escape channels. The fine structure can therefore influence the energy balance and the spectral position of the response.

The constituent and the superperiod thus play complementary roles: one supplies the waves and the other couples them into collective bands. Because coupling changes the phase accumulated across each period, the band shape also controls how a spectral feature moves with incidence angle. This relationship underlies the angular phase compensation discussed next.

3. Bulk bands and dispersion geometry

3.1. Bragg coupling and angular phase compensation

In a lossless periodic medium, a Bragg gap is an interval in which lattice-coupled waves become evanescent. Narimanov showed how this photonic-crystal mechanism can act on the short internal wavelengths of a hyperbolic constituent [3]. Anisotropy provides additional freedom to shape the resulting bands and their angular dispersion. In layered PHCs, this freedom can be used to keep a filter or resonator near its operating wavelength as the direction of illumination changes.

The mechanism can be understood by following the phase through one layered supercell. As tangential momentum increases, the longitudinal phases accumulated in its dielectric and hyperbolic blocks can change in opposite directions. Choosing block thicknesses to balance these changes reduces the total phase's angular variation. At fixed frequency, this balance is expressed by

$$\frac{\partial \Phi}{\partial k_{\parallel}} = \frac{\partial \Phi_A}{\partial k_{\parallel}} + \frac{\partial \Phi_B}{\partial k_{\parallel}} \simeq 0. \tag{5}$$

Here, Φ_A and Φ_B are the longitudinal propagation phases accumulated in the two blocks of one supercell, and $\Phi = \Phi_A + \Phi_B$ is their sum. The derivative is taken at fixed ω with respect to the tangential wavenumber $k_{\parallel} \equiv k_\tau$; the subscripts A and B identify the blocks. Compensation stabilizes the Bragg phase, while impedance contrast and material dispersion continue to shape the gap width and polarization dependence. She and colleagues investigate this balance in visible-range band-gap designs [34], and Wu and colleagues apply it to calculated near-infrared transparent bands [47]; ternary designs introduce magnetic response as an additional control [48]. The shared mechanism thus supports both reflection and transmission functions, with their usable angular ranges set by the complete finite-stack response.

For a finite resonator, the wave also acquires phase upon reflection at its boundaries. Increasing the number of periods strengthens the reflector and changes field penetration, while absorption affects the energy that survives each round trip. The operating wavelength, peak amplitude, and linewidth can therefore evolve differently with angle even when the bulk propagation phase is well compensated [34,45]. This distinction matters when translating an angle-stable band into a filter or absorber: spectral stability sets the operating wavelength, and coupling and loss determine how strongly it operates there.

Band shaping also changes the directions in which energy propagates. Huang and Narimanov used the curvature of a PHC isofrequency contour to propose a planar Veselago lens with a nearly angle-independent negative relative index [49]. Their extended study examined single- and double-source imaging together with absorption and layer-thickness variations [50]. These two studies develop one theoretical lens concept and connect its band geometry to image formation: the transmitted angular spectrum supplies the spatial information, while loss and structural errors limit how much of that information reaches the image.

Constitutive anisotropy controls another aspect of the bulk response: the geometry of an isofrequency surface. For the local uniaxial dielectric model of Eq. (1), positive principal permittivities give a closed ellipsoid, while opposite signs give an open hyperboloid. Type-I hyperbolicity has $\varepsilon_\tau > 0$ and $\varepsilon_n < 0$; type II has $\varepsilon_\tau < 0$ and $\varepsilon_n > 0$. Crossing zero in a tensor component can change the connectivity of the allowed wave-vector surface, often described as a photonic Lifshitz transition [51]. This classification characterizes the constant-frequency spectrum. Berry phases and topological band invariants describe the eigenmodes and their evolution across momentum space [52].

Magnetic composites offer additional ways to change this geometry because electric and magnetic resonances act on different polarization channels. Tuz and colleagues examined bi-hyperbolic dispersion in ferrite–semiconductor superlattices, where composition and applied field control the open branches [53]. Effective-medium calculations for ferrite–semiconductor PHCs likewise show polarization-dependent elliptic and hyperbolic regimes [54]. These results identify how a constituent can change the available propagation directions; resolving the superperiod then shows how those directions enter the collective bands. Phase-sensitive beam shifts offer a complementary probe of the resulting response [55, 56].

3.2. Conical crossings and nodal-line bands

Where coupled bands meet, their local slopes and eigenmodes become as important as the overall isofrequency geometry. Narimanov predicted finite-frequency Dirac-like dispersion in PHCs [57]. Wang and colleagues studied a related two-dimensional design with an elliptic

anisotropic host, aligning TE and TM triply degenerate points into a sixfold crossing at the Brillouin-zone center [58]. The resulting near-zero-index response for both polarizations illustrates the interest of such crossings for controlling phase accumulation. Establishing their topological character requires the symmetry and eigenmode phases that accompany the aligned bands.

The constituent can also participate through the resonances of a finite inclusion. In Zheng and colleagues' numerical design, layered HMM rods produce twisted bands with degenerate self-collimation points [59]. Here, the rod eigenmodes set the fields that can couple, and their lattice arrangement shapes the collective dispersion. Self-collimation follows from this combined band shape, connecting confinement inside an inclusion to beam propagation across many cells.

In layered PHCs, a crossing can extend into a nodal ring in the space formed by in-plane and longitudinal Bloch momenta. Hu and colleagues showed theoretically how hyperbolic phase compensation tunes the slopes around such rings, producing fourfold Dirac nodal lines with type-I, critically tilted type-III, and type-II local dispersion [33]. The tilt changes the wave trajectories available near the crossing. Its classification refers to the crossing bands; the constitutive type-I/type-II terminology describes the signs of the permittivity components. Fig. 3 places these two classifications side by side to clarify which property each one addresses.

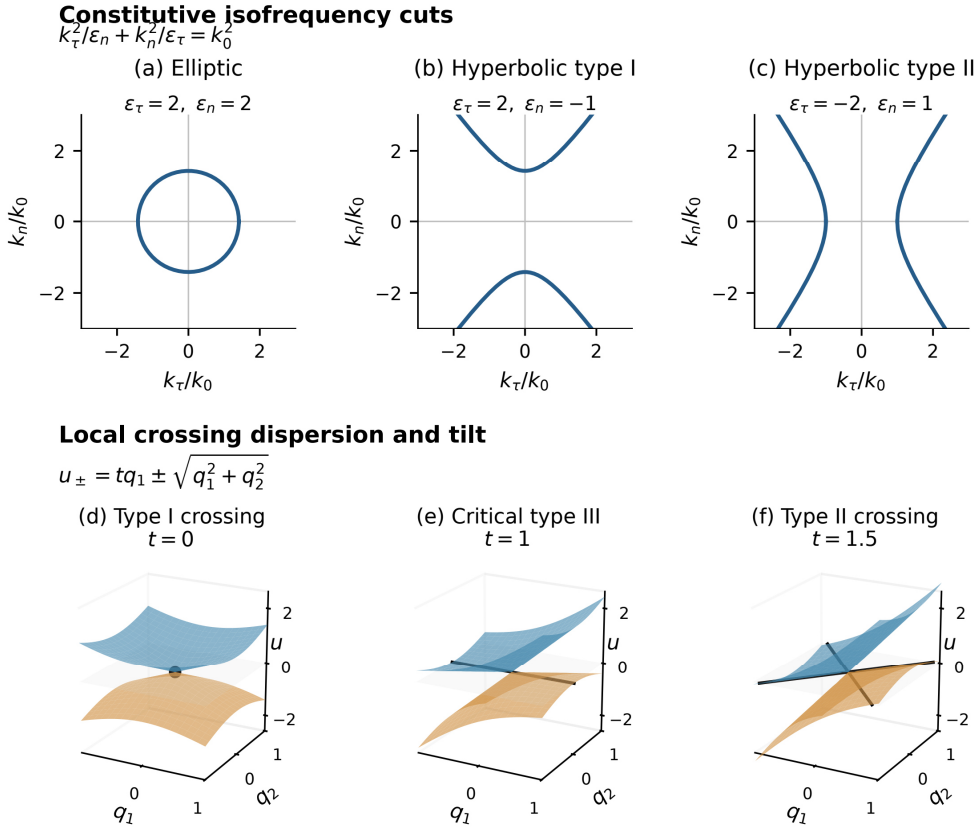


Fig. 3. Original analytical illustrations of constitutive isofrequency geometry and local band-crossing tilt. The upper row shows cuts of Eq. (1) for an elliptic medium and type-I and type-II hyperbolic media; each panel gives the dimensionless principal permittivities. The lower row plots the generic dimensionless dispersion $\boldsymbol{u}_\pm = \boldsymbol{tq}_1 \pm \left(\boldsymbol{q}_1^2 + \boldsymbol{q}_2^2\right)^{1/2}$ for tilt parameter $\boldsymbol{t} = 0$, 1, and 1.5, with dimensionless momentum coordinates $\boldsymbol{q}_1$, $\boldsymbol{q}_2$ and frequency offset $\boldsymbol{u}$. Blue and orange surfaces denote $\boldsymbol{u}_+$ and $\boldsymbol{u}_-$; their dark $\boldsymbol{u} = 0$ cuts form a point, a critical line, and crossing lines. The classifications concern tensor signs and crossing tilt, respectively [33, 51, 60]; topological invariants additionally depend on eigenmode structure and symmetry.

Conductive sheets make this band geometry adjustable. In the dielectric/graphene/metal PHC proposed by Hu and colleagues, the sheet response separates nodal rings of different polarizations and tunes their positions and tilt [60]. For the inversion-asymmetric unit cells considered there, reflection-phase singularities accompany bilateral drumhead surface states. Reducing radiative leakage and absorption brings the scattering response toward a quasi-BIC ring. This theoretical construction links a tunable bulk crossing to a boundary resonance, providing a bridge from dispersion engineering to localized fields.

The conical and nodal-line predictions illustrate the range of band structures available to PHC design [33, 57, 58, 60]. Experimental work by Orsini and colleagues on patterned hyperbolic hBN has established a deeply subwavelength topological edge state [22]. Moving from a bulk crossing to an edge mode brings the termination into the physical picture: the eigenstates of the periodic medium must meet the boundary conditions of a finite sample. The localization problem developed in the next section follows precisely this step.

For measurements, the accessible momentum range determines how much of a crossing can be traced, and loss and finite-size leakage set how sharply its branches appear. Polarization and mode symmetry help relate those features to the underlying eigenstates. Following the field toward a termination then reveals whether it continues through the bulk or becomes localized within a surrounding gap.

4. Surface, defect, and interface localization

4.1. Boundary conditions and surface-wave families

A band gap can do more than suppress propagation: it can provide the decay needed to confine a field near a defect or boundary. A localized mode is selected when this decay is compatible with tangential-field continuity and the phase accumulated between its reflectors. For a single polarization in a spacer or defect layer of thickness d, the round-trip pole condition reads

$$r_L r_R \exp(2ik_d d) = 1. \tag{6}$$

The complex amplitudes r_L and r_R are the reflection coefficients at the left and right faces of the defect, viewed from inside it. The quantity k_d is the normal propagation wavenumber in the defect, and d is its thickness; the subscript d labels that layer. With the time dependence $\exp(-\mathrm{i}\omega t)$ and outgoing exterior boundary conditions, Eq. (6) determines poles at complex frequency. Temporal decay includes leakage and absorption. In the high-reflectivity, weak-loss limit, the real-frequency resonance is approximately located by the round-trip phase,

$$\varphi_L + \varphi_R + 2\mathrm{Re}(k_d)d = 2\pi m, \qquad m \in \mathbb{Z}. \tag{7}$$

In Eq. (7), $\varphi_L = \arg r_L$ and $\varphi_R = \arg r_R$ are reflection phases, $\mathrm{Re}(k_d)$ is the real part of the defect wavenumber, and the integer m labels a longitudinal resonance order. At a direct interface, the spacer phase vanishes, leaving a match between the evanescent fields and the termination-dependent reflection or surface-impedance responses [41, 43, 61]. A matrix formulation accounts for coupled polarizations; the constitutive response and reflector determine which surface, defect, or Tamm mode satisfies the boundary condition.

The interface response provides several ways to satisfy this matching condition. Surface plasmon polaritons rely on adjacent constitutive responses, while Dyakonov-type waves use

anisotropy to achieve compatible decay over an angular range [42]. At a PHC boundary, these mechanisms can interact with decay supplied by a lattice gap. Effective-medium studies of porous-composite/PHC interfaces show how composition and temperature change plasmonic and hybrid anisotropic branches [35, 36]. Related nanocomposite calculations trace the effect of conductivity and particle filling fraction on surface-polariton dispersion [62], and PHC gap studies connect surface branches to red- and blue-shifting spectral intervals [37]. Read together, these results explain why localization depends on both the medium's response and the phase supplied by its surroundings.

Placing a conducting sheet at the boundary or using magnetic constituents makes parts of this matching condition tunable. Effective-medium calculations for graphene-based and ferrite–semiconductor PHC interfaces follow the resulting changes in propagation constants and localization [40, 63, 64]. Their tensor and sheet-current terms identify where electrical or magnetic control enters the surface-wave problem. For a state localized by a Bloch gap, the resolved periodic reflector adds the termination-dependent surface impedance. Combining these descriptions connects constituent tuning to the actual boundary at which energy is stored.

4.2. Defect resonances, Tamm states, and mode hybridization

Introducing a defect within a PHC gap creates a cavity between Bragg reflectors, so its resonance inherits both the defect propagation phase and the host reflection phases. If the host is phase-compensated, this offers a way to keep the resonance wavelength stable as the incidence angle changes. Mirror-symmetric theoretical designs use the mechanism for narrowband transmission filters [65], and a Si/ITO-based model extends it to single and coupled defects [38]. The Ag/TiO_2 defect-absorber experiment provides a useful quantitative perspective: its resonance shifted by only 3.5 nm over $0-70^{\circ}$, while peak absorptance fell from approximately 0.717 to 0.292 [45]. Thus, the cavity retained its operating wavelength as the amount of energy delivered to absorption changed substantially, a distinction directly relevant to angularly tolerant device design.

Adding a second defect couples the localized fields through their overlap. The theoretical Si/ITO model reports an avoided-crossing splitting up to 47.0 meV and frequency shifts below 1% over 0–80° [38]. The Ag/TiO_2 experiment instead probes the angular trajectory and absorptance of a fabricated defect resonance [45]. These studies connect the same phase-compensation mechanism to different observables: a calculated splitting tests interaction between two modes, while an absorption measurement tests how an incident wave delivers energy to a lossy cavity. An experimental assessment of two-mode coupling would additionally require the linewidths, mode identities, and excitation strengths across the crossing.

A metal termination offers a related localization route by replacing the internal defect with a metal–Bragg-mirror interface. The metal response and reflector supply the decay and reflection phases needed for a Tamm plasmon [43, 44]. In silver/ITO-based PHCs, Shen and colleagues measured a TM resonance that red-shifted and a TE resonance that blue-shifted as the incidence angle increased [66]. This polarization contrast shows how the dispersion of a supporting gap is inherited by an interface mode. It also suggests how the same fabricated boundary can address different spectral channels through polarization.

A further route uses the connection between bulk-band symmetry and gap impedance. For inversion-symmetric one-dimensional crystals, quantized Zak phases relate to surface

impedance when the unit-cell origin and termination are specified consistently [61]. Joining compatible gaps can then select an interface state. Theoretical HMM-containing heterostructures extend this approach to angle-insensitive and multimode resonances [67–69]. Compared with measured Tamm resonances [66], these interface-state designs add control through the adjoining lattices and their terminations, though experimental verification remains an important step.

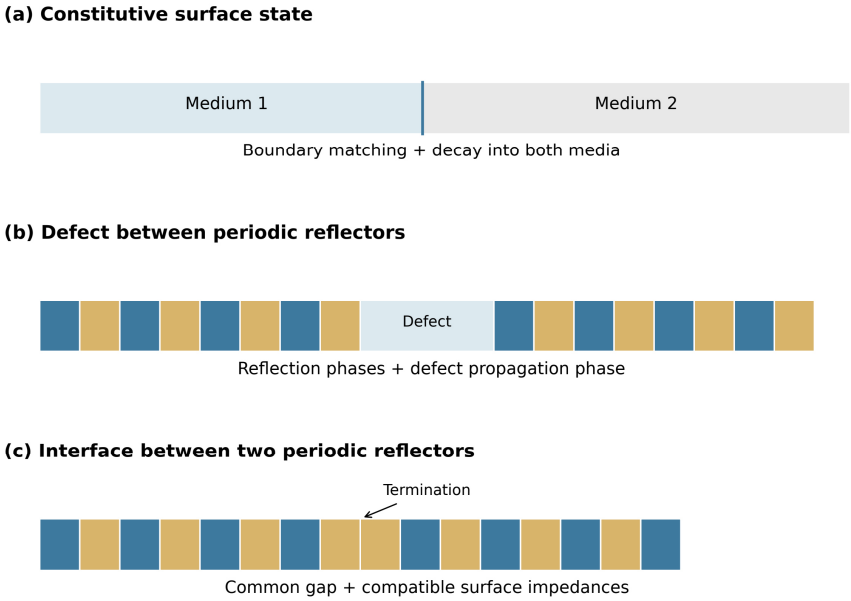


Fig. 4. Original schematic of localization geometries and matching conditions. (a) A constitutive surface state combines boundary matching with decay into both media. (b) A defect cavity combines reflection phases from two periodic reflectors with propagation through the defect. (c) A direct interface joins periodic reflectors through their termination-dependent surface impedances within a common gap. The sketches indicate interfaces and localization regions; quantitative field profiles require a mode calculation. The cited studies develop the surface-wave, Tamm-state, and gap-impedance descriptions [41–43, 61].

An added metal termination can couple an interface state to a Tamm resonance. The proposed hybrid heterostructure uses this interaction within a common gap to produce two polarization-dependent absorption branches [39]. Bulk symmetry and gap impedance establish the interface state, phase compensation shapes its angular dispersion, and coupling and dissipation determine splitting and linewidths. Fig. 4 identifies the boundaries and defect regions involved in these mechanisms. A calculated mode profile then determines its overlap with a tunable layer, an emitter, or an absorbing region, linking the localization geometry to the controls discussed next.

5. Material, boundary, and geometric control

5.1. Constitutive tuning and dissipation

Once a mode has been identified, tuning amounts to changing the part of the structure that its field samples. Magnetic bias modifies gyrotropic tensors, graphene gating changes sheet conductivity, temperature alters carrier response and damping, and gain supplies energy. These controls can move a band or resonance, change confinement, or redistribute power among excitation, absorption, and escape. Their usefulness for a particular mode depends on its spatial and polarization overlap with the region being changed.

A change in a diagonal tensor component shifts the dispersion sampled by the field and can alter frequency or confinement. Gyrotropic off-diagonal terms also affect polarization and directional response. Consequently, tuning a magnetically biased resonance can change its frequency and its scattering between the exchanged source and detector channels, linking material control to both spectral and directional measurements.

Ferrite–semiconductor PHCs illustrate this connection because ferrite and magnetoplasma resonances address magnetic and electric channels differently [31, 40, 54]. Changing the bias modifies the diagonal components and the gyrotropic terms that reverse with magnetization, thereby reorganizing propagation directions and surface branches. Which change an experiment detects depends on polarization and field orientation, together with the finite geometry that couples light to the mode. Magnetic tuning thus provides several possible controls within one material system, with the relevant one selected by the modal field.

Graphene offers electrical control within a fixed fabricated lattice. In graphene–hBN PHC calculations, changing carrier conductivity adjusts impedance matching and perfect-absorption conditions [70] and can enhance transmission in a negative-refraction regime [32]. At a graphene–magnetic-PHC boundary, electrical and magnetic parameters influence different terms of the same surface-wave problem [64]. This makes the sheet a useful boundary control: within the scalar-conductivity effective-medium description, gating shifts the spectral response without changing the physical period. The frequency, temperature, and momentum dependence of conductivity then determine the available tuning range.

Electrical control has an experimental counterpart in natural polariton media. Xu and colleagues used real-space nano-imaging of a graphene-gated α-MoO_3 hole array to measure changes in Bloch-mode intensity, wavelength, and spatial distribution [71]. The applied gate therefore acts on the collective mode as well as on its excitation. This is useful for a tunable polariton structure because a chosen bias can change where energy is concentrated and how effectively illumination reaches that region.

Evaluating such tuning requires following the field both along and away from its guiding region. For a passive mode varying as $\exp(\mathrm{i}kx)$, with $k = k' + \mathrm{i}k''$, the intensity propagation length is $L_p = 1/(2k'')$; the normal decay constants describe confinement on either side of an interface. Material absorption and field overlap can change these lengths differently. Temperature-dependent semiconductor models show how changes in carrier response affect surface-wave existence and attenuation [36]. This matters when a tuned mode is intended to carry energy over a finite distance.

Gain supplies energy where a mode overlaps an active constituent. Interface and HMM calculations explore how this reduces propagation loss [40, 72, 73]. At linear loss compensation, the supplied energy balances the calculated modal loss. Pump strength and feedback determine the subsequent operating regime and its stability. When feedback sustains a field throughout the structure, these same rates enter the lasing problem considered in Section 6.

5.2. Reciprocal geometry and nonreciprocal response

Geometry supplies a complementary set of controls. Changing period adjusts reciprocal-lattice momentum, while thickness and filling fraction alter phase and effective response; termination

modifies reflection phase. In an in-plane pattern, rotation relative to the crystal axes selects which directions of an anisotropic polariton couple to the lattice. Sahoo and colleagues demonstrated resonances controlled by pattern scale and rotation in α-MoO_3 [15]. The result shows how a fixed material can address different parts of its polariton spectrum through the fabricated geometry, offering a design choice alongside electrical or magnetic tuning.

For a linear, time-invariant structure, electromagnetic reciprocity compares power-normalized amplitudes between exchanged source and detector channels at fixed bias [74]. The comparison includes their polarization and propagation direction. In a planar structure with conserved tangential momentum, the reciprocal partner also reverses $\boldsymbol{k}_{\parallel}$: the corresponding transmission comparison is $S_{21}\left(\boldsymbol{k}_{\parallel},H\right)$ with $S_{12}\left(-\boldsymbol{k}_{\parallel},H\right)$. Symmetric constitutive tensors can support unequal reflectance and absorptance from opposite sides of an asymmetric lossy stack while retaining reciprocal transmission. Magnetic nonreciprocity is expressed in the paired-channel response of the gyrotropic constitutive model [74, 75].

Hu and colleagues combined magneto-optical response with phase compensation in a theoretical PHC absorber [76]. The bias gives its cavity mode different angular trajectories at θ and $-\theta$, and the finite lattice and defect turn that phase difference into an absorption contrast. At 367 nm, the reported absorptance is approximately 0.99 in one direction and 0.25 in the other over 20 – 75°. This illustrates the proposed function of the design: selectivity over a broad angular range emerges from directional constitutive phase together with a resonance that couples incident energy into loss.

A finite beam provides another way to observe the engineered phase. Calculations of photonic spin-Hall and Goos–Hänchen shifts use PHC gaps and graphene tuning to enhance beam displacements [55, 56]. The displacement follows phase derivatives across the beam's angular spectrum, so a sharp spectral phase variation can produce a pronounced spatial response. The beam profile and absorption determine how that response appears in a measurement. Table 3 summarizes the parameters available for controlling such phase effects alongside frequency, confinement, and attenuation.

The controls collected in Table 3 change both a mode's field distribution and its coupling to the surroundings. Their effect on a device depends on where energy is needed:

Table 3. Control parameters and their primary physical actions.

Parameter	Physical action	Response to assess	Examples
Magnetic bias	Gyrotropic permittivity and permeability	Polarization-dependent bands, surface modes, paired-channel scattering	[31, 40, 54, 76]
Graphene gating	Sheet conductivity and boundary matching	Resonance frequency, coupling, attenuation	[32, 64, 70]
Temperature	Carrier density and damping	Modal existence, dispersion, propagation length	[36]
Gain and loss	Modal energy balance	Attenuation, linewidth, feedback and stability	[40, 72, 73, 77]
Period and pattern rotation	Reciprocal momentum and optical phase	Momentum coupling, band and angular shifts	[15, 34]
Defect and termination	Cavity and reflection phase	Localization, leakage, hybridization	[38, 39, 41, 43, 66]

near an emitter, inside an absorbing layer, or throughout a nonlinear generating region. Following the energy into and out of these regions explains how the bands and localized states discussed above contribute to light–matter interaction.

6. Emitter coupling, resonant absorption, and nonlinear response

6.1. Emission, extraction, and resonant absorption

An emitter placed near a hyperbolic medium can couple to a large set of confined electromagnetic modes. The amount of energy it transfers depends on its position, dipole orientation, and spectral overlap, making the local field distribution the starting point for emission control. A PHC adds the possibility of coupling some of that energy outward through its larger lattice. In the weak-coupling regime, the dipole-projected local density of optical states describes the electromagnetic decay rate:

$$\frac{\Gamma_{\mathrm{em}}(\mathbf{r},\omega)}{\Gamma_{\mathrm{em},0}(\omega)} = \frac{\rho_{\mathbf{d}}(\mathbf{r},\omega)}{\rho_{\mathbf{d},0}(\omega)}, \qquad \Gamma_{\mathrm{em}} = \Gamma_{\mathrm{rad}} + \Gamma_{\mathrm{abs}}. \tag{8}$$

Here, Γ_{em} is the electromagnetic decay rate of an emitter at position r and angular transition frequency ω; Γ_{rad} and Γ_{abs} are its radiative and environment-absorption contributions. The local density of optical states $\rho_{\boldsymbol{d}}$ is projected along the transition dipole d. Subscript 0 denotes a reference environment with the same transition frequency and dipole. Eq. (8) assumes a weakly coupled dipole emitter. A measured inverse lifetime also includes internal nonradiative decay, whereas collected photoluminescence depends on excitation, radiative yield, and collection aperture [9, 78]. Reading lifetime and intensity together links environmental coupling to the brightness of the external source.

Periodic patterning supplies a route from a confined high-k mode to external radiation. A reciprocal vector $\boldsymbol{G}$ can shift its in-plane momentum to $\boldsymbol{k}_{\mathrm{out},\parallel} = \boldsymbol{k}_{\mathrm{mode},\parallel} + m\boldsymbol{G}$ inside the surrounding light cone. Studies of grating-assisted emission examine this combination of local interaction and momentum conversion [79, 80]. Galfsky and colleagues measured lifetime changes together with enhanced collected emission for two-dimensional semiconductor emitters and embedded quantum dots in PHCs [17, 18]. For the quantum dots, the lifetimes were 25 ns on glass, 2.97 ns in the unpatterned HMM, and 1.28 ns in the PHC [17]. The HMM comparison establishes the change produced by the hyperbolic environment; the patterned sample shows the additional contribution of the photonic lattice. Combining this lifetime comparison with collected emission gives a fuller account of decay and extraction than either observable alone.

Illumination follows the reverse energy pathway: lattice momentum can couple an incident field into a confined mode that dissipates energy. For a reflector-backed structure with one accessible radiation channel and an isolated resonance, critical coupling occurs when radiative leakage matches internal loss. The grating-coupled hBN design [81] demonstrates this balance computationally, while measurements on fabricated PHCs establish angular band and resonance control through optical spectra [19, 45, 66]. Their comparison separates a calculated matching condition from its implementation with dispersive materials, finite thickness, and fabrication error. HMM absorbers [83] provide a useful reference for identifying the additional role of PHC modulation in excitation and resonance phase.

6.2. Frequency conversion, bistability, and lasing

Frequency conversion extends the energy pathway across two frequencies. Confining the pump increases the field driving a nonlinear polarization, and the generated wave must then propagate to a collected output. For a bulk second-order medium, the source polarization and the external power efficiency of second-harmonic generation are

$$\mathbf{P}^{(2)}(2\omega) = \varepsilon_0 \boldsymbol{\chi}^{(2)}(2\omega;\omega,\omega) : \mathbf{E}(\omega)\mathbf{E}(\omega),$$
$$\eta_{\text{ext}} = \frac{P_{2\omega,\text{out}}}{P_{\omega,\text{in}}}. \tag{9}$$

In Eq. (9), $\boldsymbol{P}^{(2)}(2\omega)$ is the bulk second-order polarization at the generated angular frequency 2ω, ε_0 is the vacuum permittivity, and $\boldsymbol{\chi}^{(2)}(2\omega;\omega,\omega)$ is the second-order susceptibility tensor. The colon denotes contraction over the two Cartesian input-field indices: its component form sums $\chi^{(2)}_{ijk} E_j E_k$ over j and k, with i identifying the output polarization. The field $\boldsymbol{E}(\omega)$ is the positive-frequency coefficient in $\boldsymbol{E}(t) = \boldsymbol{E}(\omega)e^{-\mathrm{i}\omega t} + \text{c.c.}$, where c.c. denotes the complex conjugate, and the susceptibility uses the same convention. The external power efficiency η_{ext} is the collected second-harmonic power $P_{2\omega,\text{out}}$ divided by the incident pump power $P_{\omega,\text{in}}$.

The quadratic source makes pump-field concentration attractive for conversion. The detected power also depends on tensor symmetry, phase matching, coherent modal overlap, and absorption at both frequencies. A surface nonlinearity enters through a sheet polarization. The superperiod shapes the pump distribution and the generated mode, so its effect can be assessed through pump delivery, source overlap, and harmonic extraction together. Comparison with an unpatterned constituent at matched incident power and collection geometry connects the local field enhancement to the external conversion efficiency.

Theoretical PHC studies have explored this prospect through band-edge enhancement and intensity-dependent transmission [84-86]. The transfer-matrix treatment of Buranasiri and colleagues follows a second-harmonic source inside an anisotropic HMM block and its propagation through the periodic surroundings [85]. Kerr models address a different function: near a plasmon–polariton gap, the field changes the medium's response and can create bistable transmission [84]. Recent topological-hypercrystal models use related bistability in proposed optical computing elements [87]. These predictions connect field enhancement to either generating a new frequency or switching between intensity-dependent transmission states.

At an interface, this intensity dependence feeds back into the localization condition itself. Ali's theoretical PHC/nonlinear-dielectric model supports TM surface branches whose frequency range and group velocity change with the nonlinear response [88]. The field then helps set the boundary conditions that confine it, introducing optical intensity as an additional control parameter for surface propagation.

Experiments on related hyperbolic platforms clarify which parts of this conversion process are already accessible. Silver-nanorod HMMs demonstrate phase-matched second-harmonic generation [89], while patterned Au/ZnO multilayers connect harmonic output to slow-light localization and pump coupling [90]. The PHC calculations [85] additionally retain a superperiod around the generating region. Comparing these studies therefore requires

incident-power-normalized harmonic output and a constituent reference, along with the pump absorption and collection geometry. This combination would identify the gain supplied by PHC modulation and the loss incurred in delivering and extracting the two fields.

Lasing adds sustained energy supply and feedback to the confined-field problem. Janaszek and Szczepański proposed a gain-bearing distributed-feedback PHC with electrically adjustable dispersion to control the predicted lasing spectrum [77], including spatial dispersion shifts in its Bragg wavelengths and calculated thresholds [46]. Passive emission experiments establish PHC excitation and extraction pathways relevant to this development [17, 18]. The theoretical lasers build on those pathways by balancing gain, dissipation, and escape. The experimental record considered next places these proposals alongside the functions already demonstrated in fabricated structures.

7. Experimental platforms and measured observables

7.1. Artificial composites and natural polariton media

Experimental PHCs have been developed through fabrication routes that provide different kinds of control. Smolyaninova and colleagues organized cobalt-ferrofluid inclusions and achieved larger modulation with an applied magnetic field, demonstrating a reconfigurable two-scale medium [16]. Deposited multilayers offered controlled constituent thicknesses and patterned channels for emission [17, 18]. ITO-based PHCs subsequently demonstrated a broad near-infrared TM reflectance gap with a weakly shifting long-wavelength edge [19]. Silver/ITO heterostructures used angular band control to obtain opposite TE and TM shifts of Tamm resonances [66], while Ag/TiO_2 defects combined a nearly stationary resonance with angle-dependent absorption [45]. This progression shows how control of constituent layers can be extended through the superperiod to the phase and coupling of a finite resonator.

Natural van der Waals materials offer a second route by intrinsically providing a high-k spectrum [24-29]. Alfaro-Mozaz and colleagues patterned an hBN slab and used far-field spectroscopy and near-field imaging to reveal deeply subwavelength Bloch modes and period-dependent Bragg resonances [21]. Herzig Sheinfux and colleagues pushed the lattice scale to 25–160 nm in transverse hBN hypercrystals on patterned gold, directly resolving the Bloch modes [13]. In α-MoO_3, biaxial in-plane dispersion adds orientation as a design parameter: patterned structures demonstrate configurable Bloch modes and far-field access controlled by lattice geometry [14, 15]. The experimental sequence shows how a fabricated pattern can organize the material's polaritons and provide access to fields far below the free-space wavelength.

Once collective propagation is accessible, the modulation can be used to select where and in which mode the field resides. Orsini and colleagues demonstrated an hBN edge state with a reported confinement volume of $0.021\mu m^3$ and resonance quality factor above 100 [22]; graphene-gated α -MoO_3 experiments subsequently mapped electrically controlled changes in Bloch-mode intensity, wavelength, and spatial distribution [71]. Smooth Fourier-profile substrates address mode selection through a different design choice. Near-field hBN measurements show a dominant fundamental Bloch mode with reduced higher-order excitation, supported by full-wave calculations [91]. A subsequent α-MoO_3 Fourier-crystal experiment demonstrated a quasi-single-mode response in the type-I Reststrahlen band [92]. These results give modulation profile and field symmetry a practical role in selecting the collective response that illumination excites.

Table 4. Representative experimental responses in PHCs and related hyperbolic polaritonic crystals. The entries pair each experimental platform with its spectral context and quantitative response. Lifetimes, quality factors, dimensions, and absorptance describe the emission, confinement, and absorption functions of the respective structures.

Year / spectral context	Platform and probe	Measured observable	Ref.
2014 / long-wave IR	Co ferrofluid; microscopy and spectroscopy	Nanocolumn spacing ~ 20 nm and stripe period $\sim 2\mu$ m; field-dependent order	[16]
2016–2017 / visible	Patterned Ag/Al_2O_3 and emitters; lifetime / photoluminescence	QD lifetimes: glass 25 ns, HMM 2.97 ns, PHC 1.28 ns; enhanced collected emission	[17, 18]
2019 / mid-IR	hBN hole array; far- and near-field spectroscopy	$600-1200$ nm periods; Bragg resonance with estimated $Q \simeq 190$	[21]
2022 / near-IR	ITO/Nb_2O_5 PHC; reflectance / ellipsometry	Broad TM gap with a weakly shifting long-wavelength edge	[19]
2023 / near-IR	Ag/ITO-based PHC; angular reflectance	Tamm resonance: TM red shift and TE blue shift	[66]
2023 / mid-IR	Transverse hBN on patterned Au; s-SNOM	Bloch modes at $25-160$ nm lattice constants	[13]
2023–2024 / mid-IR	Patterned α -MoO_3; near-field imaging / FTIR	Configurable Bloch modes; far-field access and orientation control	[14, 15]
2024 / mid-IR	Topological hBN/Au; near-field spectroscopy	Edge-state volume $0.021\mu m^3$ and resonance $Q > 100$	[22]
2025–2026 / mid-IR	Fourier-profile hBN / α -MoO_3 on Au; near-field imaging	Fundamental-mode-dominated hBN response; quasi-single-mode α -MoO_3 response	[91, 92]
2026 / mid-IR	Graphene / patterned α -MoO_3; nano-imaging	Gate-dependent Bloch-mode intensity, wavelength, and spatial pattern	[71]
2026 / defect resonance	Ag/TiO_2 PHC; angular absorption	3.5-nm shift over $0-70^\circ$; peak absorptance $0.717 \rightarrow 0.292$	[45]

7.2. Connecting measurements to the mechanism

The measurements in Table 4 interrogate complementary stages of the optical response. Far-field reflectance and absorptance resolve resonances with accessible radiation channels; near-field maps trace confined propagation and spatial structure. Emitter lifetimes measure total decay, and steady-state intensity adds excitation and collection. A useful comparison therefore begins with the observable and its reference sample. Measured band dispersion, localized mode volume, and collected emission answer different physical questions, and their connection emerges by following energy through the same finite structure.

Patterned and unpatterned samples offer a direct way to isolate the role of modulation. In the quantum-dot study, the lifetime changes from 25 ns on glass to 2.97 ns in an HMM and 1.28 ns in the PHC [17]; the additional change accompanies pattern-enabled out-coupling and the modified optical environment. The hBN studies trace Bloch propagation and localization through spatially resolved signals [13, 21, 22]. Comparing their results requires the relevant controls: emitter position and collection aperture in the first case, and

lattice geometry, probe resolution, and tip coupling in the second. These controls explain what the measured enhancement or confinement can establish about a proposed device.

Angular compensation provides a particularly clear comparison between spectral stability and response strength. The fabricated ITO-based structures establish weakly shifting gaps and polarization-dependent Tamm trajectories [19, 66], while the Ag/TiO_2 defect absorber retains its resonance within 3.5 nm over 0–70° as peak absorptance falls from 0.717 to 0.292 [45]. Its remaining peak absorptance is about 41% of the normal-incidence value. Together, these studies show how a stable phase condition coexists with angle-dependent coupling and dissipation. Multilayer roughness and thickness errors influence that balance; natural polariton crystals face the related challenge of accessing confined modes within material-defined bands. Gate tuning and Fourier-profile selection address this access through conductivity and field symmetry [71, 91, 92]. Their practical benefit can be assessed by following output strength and linewidth across the same range used to report the resonance position.

8. Thermal transport, inverse design, and research priorities

8.1. Momentum-resolved thermal transport

The high-k spectrum also shapes energy exchange between closely spaced bodies. Near-field radiative heat transfer samples evanescent momentum channels, allowing PHC bands and surface resonances to select contributions to the exchanged thermal power. For laterally uniform planar stacks at temperatures $T_H > T_C$, separated by a vacuum gap of width L, the net radiative energy flux per unit area from the hot body to the cold body is

$$q = \int_0^\infty \frac{\mathrm{d}\omega}{2\pi}\left[\Theta(\omega,T_H)-\Theta(\omega,T_C)\right]\iint_{\mathbb{R}^2}\frac{\mathrm{d}^2\mathbf{k}_\parallel}{(2\pi)^2}\mathcal{T}(\omega,\mathbf{k}_\parallel;L). \tag{10}$$

In Eq. (10), q is the net radiative energy flux density in W m^{-2}, ω is the angular frequency, and $\boldsymbol{k}_\parallel$ is the two-dimensional wave vector parallel to the facing surfaces; $\mathrm{d}^2\boldsymbol{k}_\parallel$ integrates over its two components. The mean thermal oscillator energy is $\Theta(\omega,T)=\hbar\omega/\left[\exp(\hbar\omega/k_BT)-1\right]$, with temperature T, reduced Planck constant $\hbar$, and Boltzmann constant k_B. The labels H and C identify the hot and cold bodies. The dimensionless transmission factor $\mathcal{T}\left(\omega,\boldsymbol{k}_\parallel;L\right)$ sums the energy-transmission contributions of the polarization channels across the gap. The expression includes propagating and evanescent waves [93–95]. Finite-stack reflection operators determine their transmission; spatial dispersion becomes relevant when the dominant momenta resolve the constituent layers.

When the surface itself is patterned, diffraction couples in-plane momentum channels. The scattering formulation then follows a Bloch wave vector in the surface Brillouin zone and traces transmission over a matrix of diffraction orders [96]. This provides the connection from the planar reference expression to the patterned polariton geometries discussed earlier, retaining the momentum mixing introduced by their lattice.

Cortés-López and colleagues calculate how plasmonic PHC layers open spectral and momentum gaps and how their geometry and stacking order reshape the predicted heat flux [97]. HMM and graphene/hBN calculations provide constituent-level comparisons [98, 99]. Taken together, these studies show that the effect of modulation depends on the channels

weighted by separation and temperature, as well as on the gap-facing termination. The predicted enhancement or suppression thus belongs to a specified pair of finite structures and operating conditions. Measurement of the same geometry would connect this momentum-selective mechanism to thermal performance.

8.2. Inverse design across structural scales

The preceding examples repeatedly use several design parameters to shape one measured response. Composition, layer thickness, period, termination, and bias influence connected parts of the same mode, making inverse design a natural way to explore their combinations. A target wavelength provides an initial spectral aim; adding linewidth, external efficiency, loss, and fabrication tolerance relates that aim to an optical function. Adjoint optimization can address coupling and extraction directly, while surrogate and generative models help search the larger space of geometries with similar spectra.

Related platforms provide starting methods for this search: Maxwell-constrained prediction for multilayers [100], neural design of hyperbolic dispersion [101], and adjoint optimization of an HMM out-coupling grating [102]. The last example directly targets access to a measured channel, while the first two establish relations between material or geometric parameters and the calculated response. Nonreciprocal and thermal multilayer studies extend these strategies to broader spectral objectives [103–107]. Their relevance to a PHC lies in retaining the constituent scale, superperiod, and boundary in the forward model and checking the selected geometry with an independent resolved calculation.

A candidate geometry is assessed through forward calculations across its intended frequency, momentum, and control range. Passive material models require causal dispersion and passivity; active structures also require the gain and feedback conditions governing stability. Because several geometries can reproduce a similar spectrum, their tolerance to fabrication variations helps distinguish solutions with useful operating margins. Inverse design can therefore guide the selection of a realizable structure as well as its nominal spectral response.

8.3. Research directions

Experimental progress in emission, angular-band engineering, localized resonances, and tunable Bloch modes provides a foundation for the next stage of PHC research [13, 17, 19, 45, 66, 71]. A recurring issue is how stronger confinement changes energy exchange. Increasing the local field can strengthen an interaction and increase its exposure to material absorption, while lattice momentum and boundary coupling determine the energy that is transported or collected. Following confinement, linewidth and output power would connect this local enhancement to the improvement sought in a source, waveguide, or absorber.

For angularly stable and tunable devices, the same issue appears as a changing relationship between spectral position and response strength. A resonance can retain its wavelength as its amplitude varies with illumination; gating and Fourier-profile selection also change both the mode and its optical access. The reported experiments provide concrete starting points for examining these linked changes across a tuning range [45, 71, 91, 92]. Relating them to measured geometry and fabrication variation would help identify operating ranges that survive realistic structural deviations.

Nonlinear and active proposals extend this question to several frequencies or competing energy rates. A converter must combine pump access, coherent source overlap,

and harmonic extraction; a gain-assisted device must balance supply, dissipation, and leakage while maintaining stable operation. These requirements connect the proposed PHC switching and lasing functions to measurable input–output behavior [77, 84, 85, 87]. Nodal-band and thermal designs open further momentum-dependent functions, including control of crossing geometry and separation-dependent transmission [33, 60, 97]. Resolved electrodynamics and inverse design can help select finite structures in which these mechanisms remain accessible to excitation and measurement, defining a path from theoretical spectra to device tests.

9. Conclusions

Photonic hypercrystals connect the short internal wavelengths of hyperbolic media to collective optical functions through periodic coupling and finite boundaries. Comparing artificial multilayers with patterned natural polariton media reveals a shared sequence: the constituent supplies confined waves, the lattice reorganizes propagation, and the termination selects localization and optical access. The material and fabrication route determine how each stage is realized.

Experiments establish band control, localized resonances, changes in emitter decay and collected emission, and tunable or selectively excited polaritonic modes. Their comparison also identifies the controls needed to assign a response to modulation: an appropriate constituent reference, a defined excitation and collection geometry, and simultaneous attention to spectral position and response strength. Theoretical studies extend these mechanisms to active, nonlinear, nodal-band, and thermal functions, supplying specific finite-structure predictions for subsequent tests.

The central design question is how concentrated fields exchange useful energy. A localized mode identifies where an interaction can occur; its dissipation, leakage, and output coupling determine the accessible response. Following these quantities across a tuning or angular range connects a favorable dispersion curve to an operating device. Resolved modeling, complementary measurements, and fabrication-aware design provide the next steps toward this connection.

Funding. This work received no external funding.

Disclosures. The author declares no conflicts of interest.

Author's contributions. Illia Fedorin: conceptualization, literature analysis, methodology, numerical illustrations, and manuscript writing and editing.

References

1. Joannopoulos, J. D., Johnson, S. G., Winn, J. N., & Meade, R. D. (2008). *Photonic Crystals: Molding the Flow of Light* (2nd ed.). Princeton University Press.
2. Poddubny, A., Iorsh, I., Belov, P., & Kivshar, Y. (2013). Hyperbolic metamaterials. *Nature Photonics, 7*, 948-957.
3. Narimanov, E. E. (2014). Photonic hypercrystals. *Physical Review X, 4*, Article 041014.
4. Elser, J., Podolskiy, V. A., Salakhutdinov, I., & Avrutsky, I. (2007). Nonlocal effects in effective-medium response of nanolayered metamaterials. *Applied Physics Letters, 90*, Article 191109.
5. Kidwai, O., Zhukovsky, S. V., & Sipe, J. E. (2012). Effective-medium approach to planar multilayer hyperbolic metamaterials: Strengths and limitations. *Physical Review A, 85*, Article 053842.
6. Yan, W., Wubs, M., & Mortensen, N. A. (2012). Hyperbolic metamaterials: Nonlocal response regularizes broadband supersingularity. *Physical Review B, 86*, Article 205429.
7. Li, T., & Khurgin, J. B. (2016). Hyperbolic metamaterials: beyond the effective medium theory. *Optica, 3*, 1388-1396.
8. Orlov, A. A., Voroshilov, P. M., Belov, P. A., & Kivshar, Y. S. (2011). Engineered optical nonlocality in nanostructured metamaterials. *Physical Review B, 84*, Article 045424.

9. Kidwai, O., Zhukovsky, S. V., & Sipe, J. E. (2011). Dipole radiation near hyperbolic metamaterials: applicability of effective-medium approximation. *Optics Letters, 36*, 2530-2532.
10. Zhang, R. Z., & Zhang, Z. M. (2017). Validity of effective medium theory in multilayered hyperbolic materials. *Journal of Quantitative Spectroscopy and Radiative Transfer, 197*, 132-140.
11. Mahmoodi, M., Tavassoli, S. H., Takayama, O., Sukham, J., Malureanu, R., & Lavrinenko, A. V. (2019). Existence Conditions of High-k Modes in Finite Hyperbolic Metamaterials. *Laser & Photonics Reviews, 13*, Article 1800253.
12. Belov, P. A., & Hao, Y. (2006). Subwavelength imaging at optical frequencies using a transmission device formed by a periodic layered metal-dielectric structure operating in the canalization regime. *Physical Review B, 73*, Article 113110.
13. Herzig Sheinfux, H., Jung, M., Orsini, L., Ceccanti, M., Mahalanabish, A., Martinez-Cercós, D., Torre, I., Barcons Ruiz, D., Janzen, E., Edgar, J. H., Pruneri, V., Shvets, G., & Koppens, F. H. L. (2023). Transverse Hypercrystals Formed by Periodically Modulated Phonon Polaritons. *ACS Nano, 17*, 7377-7383.
14. Lv, J., Wu, Y., Liu, J., Gong, Y., Si, G., Hu, G., Zhang, Q., Zhang, Y., Tang, J. X., Fuhrer, M. S., Chen, H., Maier, S. A., Qiu, C. W., & Ou, Q. (2023). Hyperbolic polaritonic crystals with configurable low-symmetry Bloch modes. *Nature Communications, 14*, 3894.
15. Sahoo, N. R., Kumar, B., Prasath, S. S. J., Dixit, S., Kumar, R., Bapat, A., Sharma, P., Caldwell, J. D., & Kumar, A. (2024). Polaritons in Photonic Hypercrystals of van der Waals Materials. *Advanced Functional Materials, 34*, Article 2316863.
16. Smolyaninova, V. N., Yost, B., Lahneman, D., Narimanov, E. E., & Smolyaninov, I. I. (2014). Self-assembled tunable photonic hyper-crystals. *Scientific Reports, 4*, 5706.
17. Galfsky, T., Gu, J., Narimanov, E. E., & Menon, V. M. (2017). Photonic hypercrystals for control of light–matter interactions. *Proceedings of the National Academy of Sciences, 114*, 5125-5129.
18. Galfsky, T., Sun, Z., Considine, C. R., Chou, C. T., Ko, W. C., Lee, Y. H., Narimanov, E. E., & Menon, V. M. (2016). Broadband Enhancement of Spontaneous Emission in Two-Dimensional Semiconductors Using Photonic Hypercrystals. *Nano Letters, 16*, 4940-4945.
19. Shen, K. S., Li, X. K., Zheng, Y., Liu, H. C., Dong, S. Q., Zhang, J., Xia, S. Q., Dong, C., Sun, X. L., Zhang, X. Z., Xue, C. H., & Lu, H. (2022). Near-infrared ITO-based photonic hypercrystals with large angle-insensitive bandgaps. *Optics Letters, 47*, 917-920.
20. Hoffman, A. J., Alekseyev, L., Howard, S. S., Franz, K. J., Wasserman, D., Podolskiy, V. A., Narimanov, E. E., Sivco, D. L., & Gmachl, C. (2007). Negative refraction in semiconductor metamaterials. *Nature Materials, 6*, 946-950.
21. Alfaro-Mozaz, F. J., Rodrigo, S. G., Alonso-González, P., Vélez, S., Dolado, I., Casanova, F., Hueso, L. E., Martín-Moreno, L., Hillenbrand, R., & Nikitin, A. Y. (2019). Deeply subwavelength phonon-polaritonic crystal made of a van der Waals material. *Nature Communications, 10*, 42.
22. Orsini, L., Herzig Sheinfux, H., Li, Y., Lee, S., Andolina, G. M., Scarlatella, O., Ceccanti, M., Soundarapandian, K., Janzen, E., Edgar, J. H., Shvets, G., & Koppens, F. H. L. (2024). Deep subwavelength topological edge state in a hyperbolic medium. *Nature Nanotechnology, 19*, 1485-1490.
23. Hu, H., Teng, H., Chen, N., Xue, Z., Sun, Z., García de Abajo, F. J., & Dai, Q. (2026). Transport of polaritons in hyperbolic media. *Nature Reviews Materials, 11*, 554-574.
24. Caldwell, J. D., Aharonovich, I., Cassabois, G., Edgar, J. H., Gil, B., & Basov, D. N. (2019). Photonics with hexagonal boron nitride. *Nature Reviews Materials, 4*, 552-567.
25. Caldwell, J. D., Kretinin, A. V., Chen, Y., Giannini, V., Fogler, M. M., Francescato, Y., Ellis, C. T., Tischler, J. G., Woods, C. R., Giles, A. J., Hong, M., Watanabe, K., Taniguchi, T., Maier, S. A., & Novoselov, K. S. (2014). Sub-diffractional volume-confined polaritons in the natural hyperbolic material hexagonal boron nitride. *Nature Communications, 5*, 5221.
26. Dai, S., Fei, Z., Ma, Q., Rodin, A. S., Wagner, M., McLeod, A. S., Liu, M. K., Gannett, W., Regan, W., Watanabe, K., Taniguchi, T., Thiemens, M., Dominguez, G., Neto, A. H. C., Zettl, A., Keilmann, F., Jarillo-Herrero, P., Fogler, M. M., & Basov, D. N. (2014). Tunable phonon polaritons in atomically thin van der Waals crystals of boron nitride. *Science, 343*, 1125-1129.
27. Li, P., Lewin, M., Kretinin, A. V., Caldwell, J. D., Novoselov, K. S., Taniguchi, T., Watanabe, K., Gaussmann, F., & Taubner, T. (2015). Hyperbolic phonon-polaritons in boron nitride for near-field optical imaging and focusing. *Nature Communications, 6*, 7507.
28. Ma, W., Alonso-González, P., Li, S., Nikitin, A. Y., Yuan, J., Martín-Sánchez, J., Taboada-Gutiérrez, J., Amenabar, I., Li, P., Vélez, S., Tollan, C., Dai, Z., Zhang, Y., Sriram, S., Kalantar-Zadeh, K., Lee, S. T., Hillenbrand, R., & Bao, Q. (2018). In-plane anisotropic and ultra-low-loss polaritons in a natural van der Waals crystal. *Nature, 562*, 557-562.
29. Passler, N. C., Ni, X., Hu, G., Matson, J. R., Carini, G., Wolf, M., Schubert, M., Alù, A., Caldwell, J. D., Folland, T. G., & Paarmann, A. (2022). Hyperbolic shear polaritons in low-symmetry crystals. *Nature, 602*, 595-600.
30. Ali, M. Z. (2018). Dispersion relations and wave propagation in photonic hypercrystals. *Modern Physics Letters B, 32*, Article 1750320.

31. Fedorin, I. V. (2018). Electrodynamic properties of a hypercrystal with ferrite and semiconductor layers in an external magnetic field. *Superlattices and Microstructures, 113*, 337-345.
32. Sayem, A. A., Rahman, M. M., Mahdy, M. R. C., Jahangir, I., & Rahman, M. S. (2016). Negative Refraction with Superior Transmission in Graphene-Hexagonal Boron Nitride (hBN) Multilayer Hyper Crystal. *Scientific Reports, 6*, Article 25442.
33. Hu, S., Guo, Z., Jiang, H., & Chen, H. (2022). Photonic Dirac nodal-line semimetals realized by a hypercrystal. *Physical Review Research, 4*, Article 023047.
34. She, Y., Ruan, J., Cheng, Z., Zhao, W., Liu, Y., Huang, Y., Fang, J., Wu, X., Lu, Z., Chen, Y., Chen, Y., & Wu, F. (2024). Large angle-insensitive photonic band gap in a one-dimensional photonic hypercrystal in the visible range based on the phase-variation compensation theory. *Physics Letters A, 521*, Article 129752.
35. Fedorin, I., Khrypunova, A., & Khrypunova, I. (2018). Electromagnetic surface waves guided by a plane interface between a porous nanocomposite and a hypercrystal. *Optik, 172*, 596-606.
36. Fedorin, I. (2019). Surface electromagnetic waves at the interface between dissipative porous nanocomposite and hypercrystal under different temperatures. *Physics Letters A, 383*, Article 125863.
37. Haider, H., & Zulfiqar Ali, M. (2023). Dispersion Properties of Surface Waves Decaying in Red-Shifted and Blue-Shifted Gaps in Photonic Hypercrystals. *Advances in Condensed Matter Physics, 2023*, Article 6773192.
38. Wu, F., She, Y., Jiang, H., Liu, G., Chen, G., & Xiao, S. (2025). Angle-immune strong coupling between two defect modes in a defective photonic hypercrystal. *Optics and Lasers in Engineering, 186*, Article 108842.
39. Shen, S., Chew, X. Y., Jing, Q., Wu, X., & Dai, J. (2025). Angle-independent coupling between topological interface states and Tamm states in photonic crystal heterostructures with hyperbolic metamaterials. *Applied Physics Letters, 126*, Article 261704.
40. Fedorin, I. (2025). Dispersion properties of surface polaritons at hypercrystal-homogeneous media interface under an external magnetic field. Waves in Random and Complex Media, advance online publication, 1–24.
41. Yeh, P., Yariv, A., & Cho, A. Y. (1978). Optical surface waves in periodic layered media. *Applied Physics Letters, 32*, 104-105.
42. Takayama, O., Crasovan, L. C., Johansen, S. K., Mihalache, D., Artigas, D., & Torner, L. (2008). Dyakonov Surface Waves: A Review. *Electromagnetics, 28*, 126-145.
43. Kaliteevski, M., Iorsh, I., Brand, S., Abram, R. A., Chamberlain, J. M., Kavokin, A. V., & Shelykh, I. A. (2007). Tamm plasmon-polaritons: Possible electromagnetic states at the interface of a metal and a dielectric Bragg mirror. *Physical Review B, 76*, Article 165415.
44. Bikbaev, R. G., Vetrov, S. Y., & Timofeev, I. V. (2020). Hyperbolic metamaterial for the Tamm plasmon polariton application. *Journal of the Optical Society of America B, 37*, 2215-2220.
45. Liu, M., Lu, G., & Wang, B. (2026). Angle-Insensitive Defect-Mode Absorption in Photonic Crystals Containing Hyperbolic Metamaterials. *Nanomaterials, 16*, 985.
46. Janaszek, B., & Szczepański, P. (2022). Spatial Dispersion in Hypercrystal Distributed Feedback Lasing. *Materials, 15*, 3482.
47. Wu, F., Ruan, J., He, L., Panda, A., & Jiang, H. (2025). Angle-Dispersion-Free Near-Infrared Transparent Bands in One-Dimensional Photonic Hypercrystals. *Photonics, 12*, 748.
48. Shiveshwari, L. (2026). Omnidirectional band gap in photonic hypercrystal. Journal of Optics, 55, 955–963.
49. Huang, Z., & Narimanov, E. E. (2014). Veselago lens by photonic hyper-crystals. *Applied Physics Letters, 105*, Article 031101.
50. Huang, Z., & Narimanov, E. E. (2014). Optical imaging with photonic hyper-crystals: Veselago lens and beyond. *Journal of Optics, 16*, Article 114009.
51. Krishnamoorthy, H. N. S., Jacob, Z., Narimanov, E., Kretzschmar, I., & Menon, V. M. (2012). Topological transitions in metamaterials. *Science, 336*, 205-209.
52. Li, Z., & Gu, Q. (2024). Topological hyperbolic metamaterials. *Nanophotonics, 13*, 825-839.
53. Tuz, V. R., Fedorin, I. V., & Fesenko, V. I. (2017). Bi-hyperbolic isofrequency surface in a magnetic-semiconductor superlattice. *Optics Letters, 42*, 4561-4564.
54. Fedorin, I. (2023). The diversity of isofrequency surface topologies in a hypercrystal composed of ferrite- and semiconductor-based metamaterials. *Scientific Reports, 13*, Article 16151.
55. Xia, J., Chen, Y., & Xiang, Y. (2021). Enhanced spin Hall effect due to the redshift gaps of photonic hypercrystals. *Optics Express, 29*, 12160-12168.
56. Ali, K., Ferranti, F., Frezza, F., & Antonini, G. (2025). Enhanced control of the Goos–Hänchen shift at graphene-hyperbolic boron nitride multilayer hyper crystal. *Optics & Laser Technology, 191*, Article 113390.
57. Narimanov, E. E. (2015). Dirac dispersion in photonic hypercrystals. *Faraday Discussions, 178*, 45-59.
58. Wang, J. R., Chen, X. D., Zhao, F. L., & Dong, J. W. (2016). Full Polarization Conical Dispersion and Zero-Refractive-Index in Two-Dimensional Photonic Hypercrystals. *Scientific Reports, 6*, Article 22739.
59. Zheng, Y., Wang, Q., Lin, M., Bibbò, L., & Ouyang, Z. (2022). Twisted Bands with Degenerate Points of Photonic Hypercrystals in Infrared Region. *Nanomaterials, 12*, 1985.

60. Hu, S., Guo, Z., Liu, W., Chen, S., & Chen, H. (2024). Hyperbolic metamaterial empowered controllable photonic Weyl nodal line semimetals. *Nature Communications, 15*, 2773.
61. Xiao, M., Zhang, Z., & Chan, C. (2014). Surface Impedance and Bulk Band Geometric Phases in One-Dimensional Systems. *Physical Review X, 4*, Article 021017.
62. Ioannidis, T., Gric, T., & Rafailov, E. (2021). The Study of the Surface Plasmon Polaritons at the Interface Separating Nanocomposite and Hypercrystal. *Applied Sciences, 11*, 5255.
63. Cheng, M., Fu, P., Lin, Y., Chen, X., Chen, S., Tang, X., & Feng, S. (2018). Analysis of tunable and highly confined surface wave in the photonic hypercrystals containing graphene-based hyperbolic metamaterial. *Superlattices and Microstructures, 121*, 75-85.
64. Fedorin, I. (2026). Tunable surface electromagnetic waves at a graphene–hypercrystal boundary under magnetic bias. *Scientific Reports, 16*, 8901.
65. Li, S., Feng, G., Liu, Y., Wu, M., Zhao, X., Sun, F., Gan, Z., Chen, Z., & Yang, Y. (2024). Omnidirectional near-infrared narrowband filters based on defective mirror-symmetry one-dimensional photonic crystals containing hyperbolic metamaterials. *Optics and Lasers in Engineering, 176*, Article 108107.
66. Shen, K. S., Xia, S. Q., Zheng, Y., Dong, S. Q., Liu, H. C., Dong, C., Li, X. K., Xue, C. H., & Lu, H. (2023). Observation of polarization-dependent optical Tamm states in heterostructures containing hyperbolic metamaterials in the near-infrared region. *Results in Physics, 46*, Article 106301.
67. Wei, Q., Bi, D., Qi, X., Ren, M., & Wu, F. (2025). Angle-independent topological interface states in one-dimensional photonic crystal heterostructures containing hyperbolic metamaterials. Optics Letters, 50, 451–454. Erratum: Wei, Q., Bi, D., Qi, X., Ren, M., & Wu, F. (2025). Optics Letters, 50, 5997.
68. Ittepadan, A., Behera, J. K., & Nayak, C. (2025). Angle-independent equidistant multimode topological interface states in a 1-D photonic crystal heterostructure containing hyperbolic metamaterials. *Physics Letters A, 555*, Article 130798.
69. Ittepadan, A., & Nayak, C. (2026). Angle-independent coupled multiple topological interface-state THz absorber. *Optics Communications, 615*, Article 133262.
70. Wu, J., Jiang, L., Guo, J., Dai, X., Xiang, Y., & Wen, S. (2016). Tunable perfect absorption at infrared frequencies by a graphene-hBN hyper crystal. *Optics Express, 24*, 17103-17114.
71. Xu, J., Yu, K., Ni, X., Renzi, E. M., Zhou, L., Yin, Y., Zhou, Z., Zhao, Z., He, T., Huang, D., Park, K. D., Wang, Z., Alù, A., & Jiang, T. (2026). Dynamic tuning of Bloch modes in anisotropic phonon polaritonic crystals. *Light: Science & Applications, 15*, 41.
72. Ni, X., Ishii, S., Thoreson, M. D., Shalaev, V. M., Han, S., Lee, S., & Kildishev, A. V. (2011). Loss-compensated and active hyperbolic metamaterials. *Optics Express, 19*, 25242-25254.
73. Argyropoulos, C., Estakhri, N. M., Monticone, F., & Alù, A. (2013). Negative refraction, gain and nonlinear effects in hyperbolic metamaterials. *Optics Express, 21*, 15037-15047.
74. Caloz, C., Alù, A., Tretyakov, S., Sounas, D., Achouri, K., & Deck-Léger, Z. L. (2018). Electromagnetic Nonreciprocity. *Physical Review Applied, 10*, Article 047001.
75. Camley, R. E. (1987). Nonreciprocal surface waves. *Surface Science Reports, 7*, 103-187.
76. Hu, S., Song, J., Guo, Z., Jiang, H., Deng, F., Dong, L., & Chen, H. (2022). Omnidirectional nonreciprocal absorber realized by the magneto-optical hypercrystal. *Optics Express, 30*, 12104-12119.
77. Janaszek, B., & Szczepański, P. (2021). Distributed Feedback Laser Based on Tunable Photonic Hypercrystal. *Materials, 14*, 4065.
78. Jacob, Z., Smolyaninov, I. I., & Narimanov, E. E. (2012). Broadband Purcell effect: Radiative decay engineering with metamaterials. *Applied Physics Letters, 100*, Article 181105.
79. Lu, D., Kan, J. J., Fullerton, E. E., & Liu, Z. (2014). Enhancing spontaneous emission rates of molecules using nanopatterned multilayer hyperbolic metamaterials. *Nature Nanotechnology, 9*, 48-53.
80. Sreekanth, K. V., Krishna, K. H., De Luca, A., & Strangi, G. (2014). Large spontaneous emission rate enhancement in grating coupled hyperbolic metamaterials. *Scientific Reports, 4*, 6340.
81. Chang, Y. C., Kildishev, A. V., Narimanov, E. E., & Norris, T. B. (2016). Metasurface perfect absorber based on guided resonance of a photonic hypercrystal. *Physical Review B, 94*, Article 155430.
82. Janaszek, B., Tyszka-Zawadzka, A., & Szczepański, P. (2023). Dispersion-enabled control of photonic density of states in photonic hypercrystals. *Optics Express, 31*, 27948-27961.
83. Sreekanth, K. V., ElKabbash, M., Alapan, Y., Rashed, A. R., Gurkan, U. A., & Strangi, G. (2016). A multiband perfect absorber based on hyperbolic metamaterials. *Scientific Reports, 6*, Article 26272.
84. Ali, M. Z. (2021). Plasmon-polariton gap and associated phenomenon of optical bistability in photonic hypercrystals. *Physics Letters A, 387*, Article 127026.
85. Buranasiri, P., Plaipichit, S., Puttharugsa, C., & Wicharn, S. (2022). Recursive-formula for second-harmonic generation problem in photonic hypercrystal. *Optik, 265*, Article 169440.
86. Smolyaninov, I. I. (2019). Nonlinear optics of photonic hyper-crystals: optical limiting and hyper-computing. *Journal of the Optical Society of America B, 36*, 1629-1636.

87. Li, H., Duan, B., Zhu, T., Shan, S., Lin, L., Li, C., & Li, Z. (2026). Optical Bistability in Photonic Topological Hypercrystals and Its Applications in Photonic Neural Network. *Nanomaterials, 16*, 561.
88. Ali, M. Z. (2017). Nonlinear surface waves in photonic hypercrystals. *Physics Letters A, 381*, 2643-2647.
89. Kolmychek, I. A., Malysheva, I. V., Novikov, V. B., Leontiev, A. P., Napolskii, K. S., & Murzina, T. V. (2020). Phase-matched optical second harmonic generation in a hyperbolic metamaterial based on silver nanorods. *Physical Review B, 102*, Article 241405.
90. Li, J., Hu, G., Shi, L., He, N., Li, D., Shang, Q., Zhang, Q., Fu, H., Zhou, L., Xiong, W., Guan, J., Wang, J., He, S., & Chen, L. (2021). Full-color enhanced second harmonic generation using rainbow trapping in ultrathin hyperbolic metamaterials. *Nature Communications, 12*, 6425.
91. Menabde, S. G., Lim, Y., Voronin, K., Heiden, J. T., Nikitin, A. Y., Lee, S., & Jang, M. S. (2025). Polaritonic Fourier crystal. *Nature Communications, 16*, 2530.
92. Menabde, S. G., Lim, Y., Nikitin, A. Y., Alonso-González, P., Heiden, J. T., Noh, H., Lee, S., & Jang, M. S. (2026). Quasi-Single-Mode Polaritonic Crystal for Hyperbolic Phonon-Polaritons. Advanced Optical Materials, 14(13), e02662.
93. Polder, D., & Van Hove, M. (1971). Theory of Radiative Heat Transfer between Closely Spaced Bodies. *Physical Review B, 4*, 3303-3314.
94. Liu, X. L., Bright, T. J., & Zhang, Z. M. (2014). Application Conditions of Effective Medium Theory in Near-Field Radiative Heat Transfer Between Multilayered Metamaterials. *Journal of Heat Transfer, 136*, Article 092703.
95. Liu, R., Zhou, C., Zhang, Y., Cui, Z., Wu, X., & Yi, H. (2022). Near-field radiative heat transfer in hyperbolic materials. *International Journal of Extreme Manufacturing, 4*, Article 032002.
96. Messina, R., Noto, A., Guizal, B., & Antezza, M. (2017). Radiative heat transfer between metallic gratings using Fourier modal method with adaptive spatial resolution. *Physical Review B, 95*, Article 125404.
97. Cortés-López, S., Castillo-López, D. N., Espinoza-Merino, A., & Castillo-López, S. G. (2025). Momentum and spectral bandgaps: shaping the near-field radiative heat transfer between plasmonic hypercrystals. *Optics Express, 33*, 46861-46872.
98. Guo, Y., & Jacob, Z. (2013). Thermal hyperbolic metamaterials. *Optics Express, 21*, 15014-15019.
99. Zhao, B., Guizal, B., Zhang, Z. M., Fan, S., & Antezza, M. (2017). Near-field heat transfer between graphene/hBN multilayers. *Physical Review B, 95*, Article 245437.
100. Lynch, S., LaMountain, J., Fan, B., Bu, J., Raju, A., Wasserman, D., Karpatne, A., & Podolskiy, V. A. (2025). Physics-Guided Hierarchical Neural Networks for Maxwell's Equations in Plasmonic Metamaterials. *ACS Photonics, 12*, 4279-4288.
101. Shi, Y. C., Chen, J., Ding, W., Zhao, M., Wu, H., Xu, K., & Wu, R. X. (2025). Deep Learning for On-Demand Hyperbolic Dispersion in Metasurfaces. *ACS Photonics, 12*, 5994-6001.
102. Ma, H., Bao, G., Lai, J., & Lin, J. (2024). Inverse design of a grating metasurface for enhancing spontaneous emission through hyperbolic metamaterials. *Journal of the Optical Society of America B, 41*, A79-A85.
103. Zhang, W., Pan, H., & Wang, S. (2026). Deep learning based inverse design of nonreciprocal multilayer photonic structures. *Journal of Optics*, *28*(6), Article 065101.
104. Chen, Z., & Hu, R. (2025). Strong Nonreciprocal Broadband Thermal Radiation via Materials Informatics Inverse Design. *Advanced Optical Materials*, *13*(28), e01219.
105. Sui, J. Y., & Zhang, H. F. (2026). Inverse design epsilon-near-zero-based broadband nonreciprocal thermal emitter using hybrid deep learning framework. *Applied Physics Letters*, *128*(13), Article 133902.
106. Liao, T., Zhao, C. Y., Wang, H., & Ju, S. (2024). Data-driven design of multilayer hyperbolic metamaterials for near-field thermal radiative modulator with high modulation contrast. *International Journal of Heat and Mass Transfer, 219*, Article 124831.
107. García-Esteban, J. J., Cuevas, J. C., & Bravo-Abad, J. (2024). Generative adversarial networks for data-scarce radiative heat transfer applications. *Machine Learning: Science and Technology, 5*, Article 015060.

Fedorin, I. (2027). Photonic Hypercrystals: Multiscale Dispersion, Localization, and Optical Control. Review. *Ukrainian Journal of Physical Optics*, *28*(2), 02001 – 02025.
doi: 10.3116/16091833/Ukr.J.Phys.Opt.2027.02001

Анотація. *В огляді розглянуто, як періодична модуляція перетворює сильно локалізовані хвилі гіперболічних середовищ на колективні зони, локалізовані стани та доступний для оптичного збудження відгук. Штучні багатошарові структури й періодично модульовані природні поляритонні середовища зіставлено за роллю дисперсії складових, взаємодії через ґратку та граничних умов. Фізичні механізми пов'язані з виміряними зміщеннями зон, часами життя емітерів, поглинанням і ближньопольовими картами мод. Розглянуто контрольні порівняння, необхідні для*

встановлення внеску періодичності. Експерименти підтверджують низку функцій поширення та локалізації, а теоретичні дослідження розширюють можливості проєктування на нелінійне перетворення, підсилення, вузлові зони й теплоперенесення. Зіставлення цих результатів виявляє спільний компроміс: концентрація поля посилює локальну взаємодію, тоді як дисипація та зв'язок із зовнішніми каналами визначають енергію корисного вихідного сигналу. Такий підхід пов'язує багатомасштабне дисперсійне проєктування з експериментальними спостереженнями й окреслює завдання щодо скінченних структур, керованості та стійкості до похибок під час виготовлення.

Ключові слова: *фотонні гіперкристали, гіперболічні метаматеріали, поляритонні кристали, блохівські моди, оптична локалізація, взаємодія світла та речовини*